Biomaterials Science

Accepted Manuscript

This article can be cited before page numbers have been issued, to do this please use: X. Fu, X. Zhao, L. Chen, P. Ma, T. Liu and X. Yan, *Biomater. Sci.*, 2023, DOI: 10.1039/D3BM00142C.

ROYAL SOCIETY OF CHEMISTRY

rsc.li/biomaterials-science

View Article Online
DOI: 10.1039/D3BM00142C

ARTICLE

Mesoporous polyacrylic acid/calcium phosphate coated persistent luminescence nanoparticles for improved afterglow bioimaging and chemotherapy of bacterial infection

Received 00th January 20xx,
Accepted 00th January 20xx

DOI: 10.1039/x0xx00000x

Xuan Fu,[abc] Xu Zhao,[abc] Li-Jian Chen,[abc] Piming Ma,[d] Tianxi Liu,[de] and Xiu-Ping Yan *[abcd]

Coating mesoporous drug carriers on the surface of persistent luminescence nanoparticles (PLNPs) not only allows continuous luminous imaging without spontaneous fluorescence interference, but also provides drug release guidance. However, in most cases, the encapsulation of the drug-loaded shells significantly reduces the luminescence of PLNPs, which is unfavorable for bioimaging. In addition, conventional drug-loaded shells alone, such as silica shells, are difficult to achieve responsive fast drug release. Here, we report the fabrication of mesoporous polyacrylic acid (PAA)/calcium phosphate (CaP) shell-coated PLNPs (PLNPs@PAA/CaP) for improved afterglow bioimaging and drug delivery. The encapsulation of the PAA/CaP shell effectively prolonged the decay time and enhanced the sustained luminescence of PLNPs by about three times due to the passivation of the surface defects of PLNPs by the shell, and the energy transfer between the shell and PLNPs. Meanwhile, the mesoporous structure and negative charge of the PAA/CaP shells enabled the prepared PLNPs@PAA/CaP to carry the positively charged drug doxycycline hydrochloride efficiently. Under the acidic conditions of bacterial infection, the degradation of PAA/CaP shells and the ionization of PAA permitted fast drug release for effective killing of bacteria at the infection site. The excellent persistent luminescence properties, outstanding biocompatibility, and rapid responsive release feature make the prepared PLNPs@PAA/CaP a promising nanoplatform for diagnostic and therapeutic applications.

Introduction

Persistent luminescence nanoparticles (PLNPs) can store excitation energy in inherent defects upon excitation and release stored charge carriers in response to heat or other stimuli, resulting in luminescence lasting minutes, or even days after excitation stops.[1,2] Contrary to fluorescence that depends on real-time excitation, persistent luminescence is not affected by excitation light-induced scattering and autofluorescence.[3] Therefore, PLNPs are considered as excellent luminescent nanoparticles for ultrasensitive luminescence detection with high signal to background contrast in biosensing,[4] in vivo deep tissue imaging,[5,6] drug delivery,[7] cancer treatment diagnosis,[8,9] and antibacterial treatment diagnosis.[10,11]

The existing fabrication of core-shell PLNPs for drug delivery usually suffers a few problems. The conversion of large-sized bulky persistent luminescence powders to nanosized PLNPs leads to many surface defects that can quench the luminescence of the materials.[12] A series of operations, such as hydroxylation and modification with silane reagent, are often needed before the surface of PLNPs is coated with shells. These operations also often impair the luminescence performance of PLNPs. In addition, the coating of mesoporous shells on the surface of PLNPs for drug delivery usually impairs the luminescent performance of PLNPs further.[13,14] Therefore, the synthesis of the shells with both enhanced luminescence and drug loading function is very imperative for theranostic purpose.

Polyacrylic acid (PAA), a non-toxic, biocompatible and biodegradable polymer, is usually used to replace the original hydrophobic ligand on the surface of nanocrystals to achieve phase transfer of water-soluble nanocrystals.[15,16] The abundant carboxyl group of PAA makes PAA grafted nanoparticles hydrophilic and effective to load some drugs through electrostatic interaction.[17] Calcium phosphate (CaP), an inorganic mineral similar to natural bone, has high biocompatibility and biodegradability.[18,19] The structure composed of PAA and CaP is an ideal choice for drug delivery and antibacterial applications due to its acid degradation responsive characteristics.[20,21] It is very interesting that the coating of the PAA/CaP shell was found to effectively enhance the fluorescence of gold clusters.[22] However, the coating of PAA/CaP also led to the blue shift of the fluorescence emission of gold clusters from red to bright yellow, deviating from the near infrared optical window.[22] Thus, integrating the good signal penetrability and spontaneous fluorescence interference-free nature of NIR-emitting

[a] State Key Laboratory of Food Science and Technology, Jiangnan University, Wuxi, 214122, China
[b] International Joint Laboratory on Food Safety, Jiangnan University, Wuxi 214122, China
[c] Institute of Analytical Food Safety, School of Food Science and Technology, Jiangnan University, Wuxi, 214122, China
[d] Key Laboratory of Synthetic and Biological Colloids, Ministry of Education, Jiangnan University, Wuxi, 214122, China
[e] School of Chemical and Material Engineering, International Joint Research Laboratory for Nano Energy Composites, Jiangnan University, Wuxi 214122, China
†Electronic Supplementary Information (ESI) available: additional figures Fig S1-S21. See DOI: 10.1039/x0xx00000x

PLNPs to the interesting luminescence enhancement phenomenon of PAA/CaP shell may be a good idea for an amplified NIR afterglow bioimaging along with drug delivery.

Herein, we report the fabrication of a nanocarrier with PAA/CaP as the shell and NIR-emitting PLNPs as the core (named as PLNPs@PAA/CaP) for improved afterglow bioimaging and drug delivery. $Zn_{1.25}Ga_{1.5}Ge_{0.25}O_4$:0.5%Cr,2.5%Yb,0.25%Er PLNPs is used as the core for afterglow imaging due to its excellent persistent NIR luminescence performance.[23] The mesoporous structure of PAA/CaP shell is wrapped on the surface of PLNPs to load a model drug doxycycline hydrochloride (DOX) and to enhance the persistent luminescence of PLNPs. In addition, the PAA/CaP shell can be degraded in the acidic wound microenvironment to release the loaded drug. The developed DOX-loaded PLNPs@PAA/CaP (PLNPs@PAA/CaP-DOX) enables background-free afterglow imaging for luminescence imaging-guided drug delivery and bacteria killing.

Experimental

Chemicals and materials

Isopropyl alcohol (IPA), $Na_2HPO_4{\cdot}12H_2O$, $NaH_2PO_4{\cdot}2H_2O$, and $Ca(OH)_2$, GeO_2 (99.999%) came from Sinopharm Chemical Reagent Co. (Shanghai, China). $Zn(NO_3)_2{\cdot}6H_2O$ (99.99%), Ga_2O_3 (99.99%), $Cr(NO_3)_3{\cdot}9H_2O$ (99.99%), $Yb(NO_3)_3{\cdot}5H_2O$ (99.9%), $Er(NO_3)_3{\cdot}5H_2O$ (99.9%), dimethyl sulfoxide, DOX, and PAA (Mw, *ca*. 1800) were provided by Aladdin (Shanghai, China). Phosphate-buffer saline (PBS) buffer (premixed powder), hyaluronidase, Luria Bertani (LB) broth powder (FMB Grade), and LB agar powder (FMB Grade) were provided by Shanghai Sangon Biotech (Shanghai, China). Calcein-AM/PI Double Stain Kit was purchased from Yeason Biotechnology Co. (Shanghai, China).

Characterization

A JEM-2100 transmission electron microscope (JEOL, Japan) was used to obtain transmission electron microscopy (TEM) images. A JEM-F200 high-resolution transmission electron microscope was used to obtain elemental mapping images (JEOL, Japan). An F-7000 spectrofluorometer (Hitachi, Japan) was used for luminescence measurements. A UV-3600plus spectrophotometer (Shimadzu, Japan) was used to acquire UV-vis absorption spectra. A Nicolet IS10 spectrometer with a KBr pellet (Thermo Scientific, U.S.A) was employed to obtain Fourier transform infrared (FT-IR) spectra. A Nano-ZSE Zetasizer (Malvern, U.K.) was used to get hydrodynamic size distribution and Zeta potential. A D2 PHASER diffractometer (Bruker, Germany) was used to obtain X-ray diffraction (XRD) pattern. Autosorb-iQ (Quantachrome, USA) was used for N_2 adsorption experiments at 77 K. An IVIS Lumina XRMS Series III Imaging System (Perkin Elmer, USA) was used for luminescence imaging. A Q500 TG instrument (TA, USA) was used for thermogravimetric analysis (TGA) at a heating rate of 10°C min^{-1} from 25°C to 800°C under N_2 atmosphere. Fluorescent bacterial staining was acquired on an FV3000 confocal laser scanning microscope (Olympus, Japan).

Synthesis of PLNPs, PLNPs@PAA/CaP, and PLNPs@PAA

The PLNPs, $Zn_{1.25}Ga_{1.5}Ge_{0.25}O_4$:0.5%Cr,2.5%Yb,0.25%Er, was synthesized according to our previous work.[23] For subsequent synthesis of PLNPs@PAA/CaP, PLNPs aqueous solution (80 mL, 0.625 mg mL^{-1}) was added to PAA aqueous solution (20 mL, 20 mg mL^{-1}) in a 500 mL flask, and the mixture was gently stirred overnight. $Ca(OH)_2$ (130 mg) was added to the mixture and treated with ultrasound for 0.5 h. IPA (150 mL) was then dripped into the flask under magnetic stirring and kept stirring for 1 h. Afterwards, $Na_2HPO_4{\cdot}12H_2O$ aqueous solution (2 mL, 525 mg mL^{-1}) was dripped into the flask under magnetic stirring, then the mixture was stirred overnight. The product PLNPs@PAA/CaP was collected by centrifugation at 10000 rpm for 10 min and washed with ultrapure water three times.

PLNPs@PAA was also synthesized as described below for comparison. PLNPs aqueous solution (0.625 mg mL^{-1}, 80 mL) was added to PAA aqueous solution (20 mL, 20 mg mL^{-1}) in a 500 mL flask, and the mixture was gently stirred overnight. The pH of the mixture solution was adjusted to 9 with $NH_3{\cdot}H_2O$. Then, 150 mL IPA was dropped into the flask under magnetic stirring, and the mixture solution was stirred for 1 h. The product PLNPs@PAA was collected by centrifugation at 10000 rpm for 10 min.

Drug loading and in vitro release test

DOX solution (0.5 mL, 1 mg mL^{-1}) was added to PLNPs@PAA/CaP solution (0.5 mL, 2 mg mL^{-1}) and the mixture was stirred at room temperature for different times. Subsequently, the resulting PLNPs@PAA/CaP-DOX was centrifuged at 10000 rpm for 15 min. The supernatant was collected and the amount of DOX loaded into the PLNPs@PAA/CaP was measured by UV–vis spectrophotometry at 345 nm to calculate the loading capacity and loading efficiency for DOX according to Equation (1) and (2):

$$\text{Loading capacity} = \frac{M_{\text{Total DOX}} - M_{\text{DOX in supernatant}}}{M_{\text{PLNP@PAA/CaP}}} \quad (1)$$

$$\text{Loading efficiency}\ (\%) = \frac{M_{\text{Total DOX}} - M_{\text{DOX in supernatant}}}{M_{\text{Total DOX}}} \times 100\% \quad (2)$$

where $M_{PLNP@PAA/CaP}$, $M_{Total\ DOX}$ and $M_{DOX\ in\ supernatant}$ are the amounts of PLNP@PAA/CaP, total DOX inputs, and the DOX in supernatant.

For drug release experiments, the prepared PLNPs@PAA/CaP-DOX (2 mg as PLNPs@PAA/CaP) was redispersed in PBS (2 mL, 10 mmol L^{-1}, pH 7.4 and pH 5.5), and shaken at 37°C in the dark. At given time points, the solution was centrifuged, 1 mL of supernatant was collected to measure the absorbance at 345 nm, and 1 mL of fresh PBS (10 mmol L^{-1}) with the same pH value was added to the system.

Cytotoxicity assay

The cytotoxicity of the synthesized materials was evaluated by the MTT assay. 3T3 cells were seeded in the 96-well plates at a density of 1×10^4 cells per well and cultivated for 24 h. Then, the medium was removed and replaced by the fresh DMEM medium including various concentrations of PLNPs@PAA/CaP (0, 10, 50, 100, 250, and 500 μg mL^{-1}). After 24 h, the cells were washed with PBS (10 mmol

L^{-1}, pH 7.4) three times and incubated in 100 μL of the fresh DMEM medium containing MTT (0.5 mg mL^{-1}) for another 4 h. After that, dimethyl sulfoxide (100 μL) was added to each well to replace the medium and the absorbance at 490 nm was measured on a microplate reader.

Hemolysis test

Fresh blood was collected from Balb/c mice in an anticoagulant tube and centrifuged at 3000 rpm for 10 min. The centrifuged blood was diluted with PBS (10 mmol L^{-1}, pH 7.4) and mixed with different concentrations of PLNPs@PAA/CaP (0, 10, 50, 100, 250, and 500 μg mL^{-1}) and incubated at 37°C for 1 h. The samples were centrifuged at 3000 rpm for 10 min to remove erythrocytes and partial PLNPs@PAA/CaP. The supernatant was further centrifuged at 10000 rpm for 10 min to remove residual PLNPs@PAA/CaP. The hemolytic activity of PLNPs@PAA/CaP was determined by measuring the OD of the supernatant at 540 nm. The percent hemolysis was calculated according to Equation (3).

$$\text{Hemolysis rate } (\%) = \frac{OD_s - OD_n}{OD_p - OD_n} \times 100\% \quad (3)$$

where OD_S, OD_P, and OD_n are the absorbance of the sample suspension, positive control (erythrocytes in water), and negative control (erythrocytes in PBS), respectively.

Bacterial culture and in vitro antibacterial experiments

Methicillin-resistant S. aureus (MRSA) was incubated in LB broth at 37°C for 12 h. Then, the bacterial broth was centrifuged and resuspended in LB broth (pH 5.5 and 7.4) to adjust the bacterial concentration to 2×10^8 CFU mL^{-1}. 500 μL LB broth (pH 5.5 and 7.4) containing different amounts of PLNPs@PAA/CaP-DOX was mixed with 500 μL LB broth (pH 5.5 and 7.4) containing 2×10^8 CFU MRSA cells and incubated for 24 h. The turbidity of the samples was evaluated at different times by measuring the optical density at 600 nm on a multifunctional microplate reader. The bacterial suspension after 24 h culturing was serially diluted with PBS (10 mmol L^{-1}, pH 7.4), and 100 μL of each diluted sample was plated on plates and incubated at 37°C for 12 h. Finally, the colonies formed on the plates were counted to assess the bacterial concentration. To further test the antibacterial effect of PLNPs@PAA/CaP-DOX, the bacteria were stained with Calcein-AM /PI staining kit after different treatments. Briefly, the different treated bacteria were incubated with 50 μL Calcein-AM (2 μmol L^{-1}) and 50 μL PI (3 μmol L^{-1}) for 15 min, then centrifugated and resuspended in PBS (10 mmol L^{-1}). 10 μL of the bacteria resuspension was aspirated onto a slide and then imaged by confocal laser scanning microscopy.

In vivo antibacterial therapy

All animal procedures were performed in accordance with the Guidelines for Care and Use of Laboratory Animals of Jiangnan University and approved by the Animal Ethics Committee of Jiangnan University (JN.No. 20211215b0250115[540]). To construct a subcutaneous abscess model, 1×10^8 MRSA cells were subcutaneously injected into the back of each mouse. After one day of MRSA infection, the mice were randomly distributed among the groups (five mice for each group) with different treatments: PBS (200 μL, 10 mmol L^{-1}, pH 7.4), PLNPs@PAA/CaP (200 μL, 4 mg mL^{-1}), and PLNPs@PAA/CaP-DOX (200 μL, 4 mg mL^{-1} as PLNPs@PAA/CaP). Photographs of the wounds were recorded on days 0, 2, 4, 6, 8, and 10, and the area of the wounds was measured using Image J software. The body weight of the mice was recorded daily during treatment. On day 10, all mice were sacrificed, then wound tissues and major organs (heart, liver, spleen, lung, and kidney) were collected. Then, the collected wound tissues and major organs were immersed in 4% paraformaldehyde for further histological and immunological analysis of tissue sections. Tissue sections were technically supported by Erwan Biological Co. (Suzhou, China). To further compare the therapeutic effects of DOX only and PLNPs@PAA/CaP-DOX, the MRSA-infected mice were treated with PBS (200 μL, 10 mmol L^{-1}, pH 7.4), DOX (200 μL, 1.7 mg mL^{-1}). For fair comparison, the amount of DOX used is the same as the amount of DOX loaded by PLNPs@PAA/CaP-DOX (200 μL, 4 mg mL^{-1} as PLNPs@PAA/CaP). The photographs of the wounds were recorded on days 0, 2, 4, 6, 8, and 10, and the area of the wounds was measured using Image J software.

In vivo afterglow imaging

To compare the in vivo afterglow imaging ability of PLNPs and PLNPs@PAA/CaP, PLNPs and PLNPs@PAA/CaP (0.2 mL, 1 mg mL^{-1} as PLNPs) were subcutaneously injected on the back of athymic nude mice, separately. Then, the afterglow images of the mice were collected at different time points (5 min, 1 h, and 24 h). To obtain the afterglow luminescence signal during drug delivery, afterglow images of infected Balb/c mice were acquired at different time points (5 min, 30 min, 1 h, 12 h, 24 h) after PLNPs@PAA/CaP-DOX was intravenously injected. All the mice were illuminated with LED light (650 ± 10 nm, 5000 lumens) for 2 min before acquiring the images.

Results and discussion

Design and characterization of PLNPs@PAA/CaP

Fig. 1 shows the design and fabrication of PLNPs@PAA/CaP-DOX for enhanced afterglow imaging and chemotherapy. $Zn_{1.25}Ga_{1.5}Ge_{0.25}O_4$:0.5%Cr, 2.5%Yb, 0.25%Er was used as the PLNPs core to provide excellent afterglow performance. The PLNPs core was first grafted by PAA via the electrostatic interaction between PLNPs and PAA and the coordinate bonds between the surface metal ions (such as Zn^{2+} and Ga^{3+}) on the PLNPs and the -COOH group in PAA. $Ca(OH)_2$ then reacted with free PAA and PLNPs@PAA to generate PAA-Ca^{2+} and PLNPs@PAA-Ca^{2+} through acid-base neutralization reaction. Isopropanol made PAA-Ca^{2+} self-assemble around PLNP@PAA-Ca^{2+}. Finally, $Na_2HPO_4 \cdot 12H_2O$ was introduced as phosphate anion source to produce mesoporous PAA/CaP shell on the surface of the PLNPs. The effects of the dosages of PLNPs, $Ca(OH)_2$ and IPA were investigated to obtain relatively uniform spherical PLNPs@PAA/CaP (Fig. S1-S3). As such, PLNP@PAA/CaP with high drug-load capacity and pH-sensitive drug delivery was fabricated for enhanced afterglow imaging-guided infection therapy.

View Article Online
DOI: 10.1039/D3BM00142C

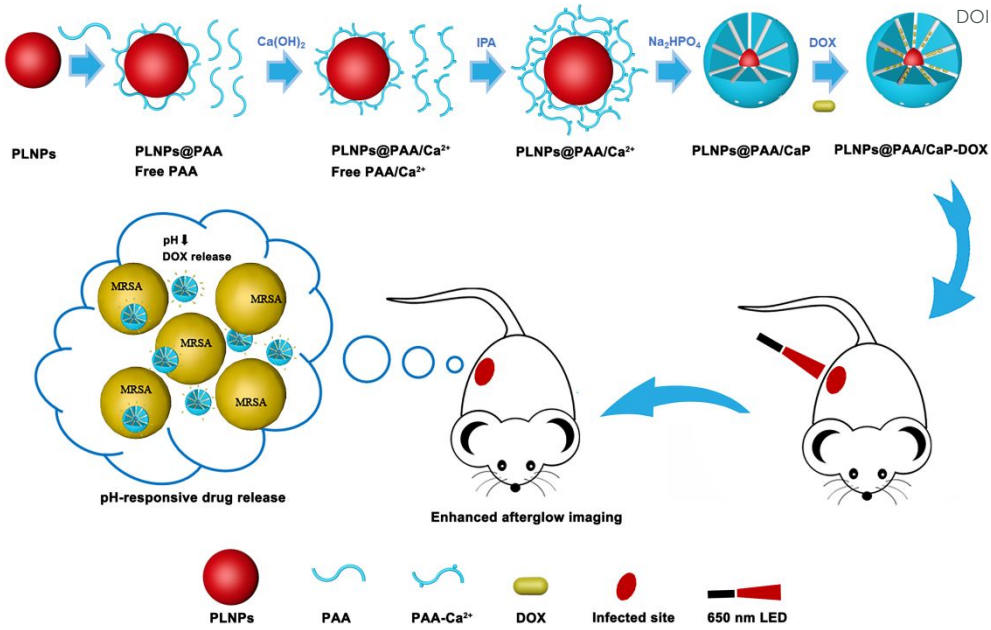

Fig. 1 Schematic for the preparation of the drug-loaded PLNPs@PAA/CaP for enhanced afterglow imaging-guided infection therapy.

The as-synthesized PLNPs were monodispersed with the particle diameter of 12.7 ± 2.0 nm (Fig. 2A and Fig. S4A). TEM image (Fig. 2B), HAADF-STEM (Fig. 2C), and EDS element mapping images (Fig. 2D-H) confirmed the core-shell structure of PLNPs@PAA/CaP. The coating of PAA/CaP on the shell of PLNPs made the mean hydrated size of the nanoparticles increase from 28 nm to 215 nm (Fig. S4B). The appearance of the O–P–O bending at 585 cm^{-1}, the asymmetric stretching of PO_4^{3-} at 1073 cm^{-1}, and the C=O of the $-COO^-$ group at 1409 cm^{-1} and 1561 cm^{-1} in FT-IR spectra of the PLNPs@PAA/CaP (Fig. S5A) further shows the presence of PAA/CaP shell.[24] UV-vis spectra reveal that the absorbance of the synthesized material increased significantly with the coating of the PAA/CaP shell (Fig. 3A). The surface composition of PLNPs@PAA/CaP was characterized by XPS (Fig. S5B). The peaks at 187 eV and 130 eV were attributed to P 2p and P 2s, respectively.[25] The peaks at 436 eV and 344 eV were assigned to Ca 2s and Ca 2p for Ca^{2+}, respectively, while the peak at 531 eV was attributed to O 1s.[26]

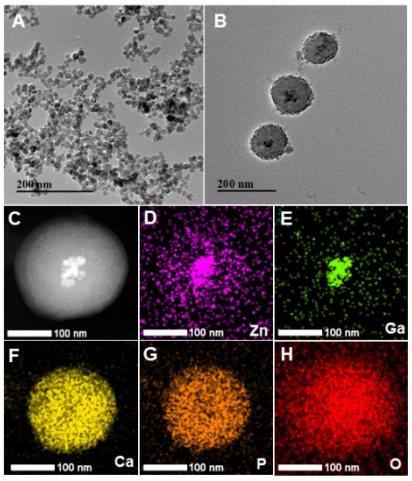

Fig. 2 TEM images of (A) PLNPs, (B) PLNPs@PAA/CaP, (C) HAADF-STEM images, (D-H) EDS element mapping images of a single PLNPs@PAA/CaP.

The diffraction peaks at 18.3°, 30.5°, 35.8°, 37.5°, 43.1°, 53.5°, 56.8°, and 62.6° in Fig. S5C show a fine cubic spinel structure of the prepared PLNPs@PAA/CaP, corresponding to the standards of Zn_2GeO_4 (JCPDS 25-1018) and $ZnGa_2O_4$ (JCPDS 38-1240).[27,28] The positions of the diffraction peaks are consistent, and the peak between 25°-35° indicates an amorphous CaP shell. The prepared PLNPs@PAA/CaP showed the Brunauer–Emmett–Teller (BET) surface area of 143.5 $m^2\ g^{-1}$ along with the pore size of *ca* 5.0 nm (Fig. S5D and S5E). Furthermore, the mass percentage of PLNPs in PLNPs@PAA/CaP was determined to be 54.8% by TGA (Fig. S5F). The above results confirm the successful preparation of PLNPs@PAA/CaP.

Enhanced persistent luminescence of PLNPs@PAA/CaP

Compared with PLNPs, the prepared PLNPs@PAA/CaP exhibited stronger absorption (Fig. 3A) and gave three times brighter luminescence than the PLNPs at 700 nm (Fig. 3B). PLNPs@PAA/CaP also offered stronger afterglow luminescence and longer afterglow time regardless of the excitation by a 254 nm UV light (Fig. 3C) or a 650 nm LED lamp (Fig. S6A). Moreover, PLNPs@PAA/CaP gave stronger reactivated afterglow than the PLNPs by a 650 nm LED lamp (Fig. 3C). However, both PLNPs@PAA/CaP and PLNPs showed similar afterglow decay rate (Fig. S6B). In addition, PLNPs@PAA/CaP showed good NIR rechargeability, demonstrating the potential of PLNPs@PAA/CaP in biological imaging (Fig. S7).

In vivo experiments were performed to further reveal the enhanced persistent luminescence of PLNPs@PAA/CaP. For this purpose, PLNPs and PLNPs@PAA/CaP were subcutaneously injected into mice separately, and the images were collected at different time points after injection (Fig. 3D). The afterglow signal from PLNPs could eliminate autofluorescence interference, and improve the imaging sensitivity. In addition, PLNPs@PAA/CaP showed much stronger afterglow than PLNPs (*ca* 3 times). Both in vitro and in vivo experiments show that the encapsulation of a PAA/CaP shell layer

can effectively enhance the persistent luminescence and improve the imaging sensitivity of PLNPs. The longer and stronger reactivatable persistent luminescence makes PLNPs@PAA/CaP promising for real-time tracking of drugs delivery.

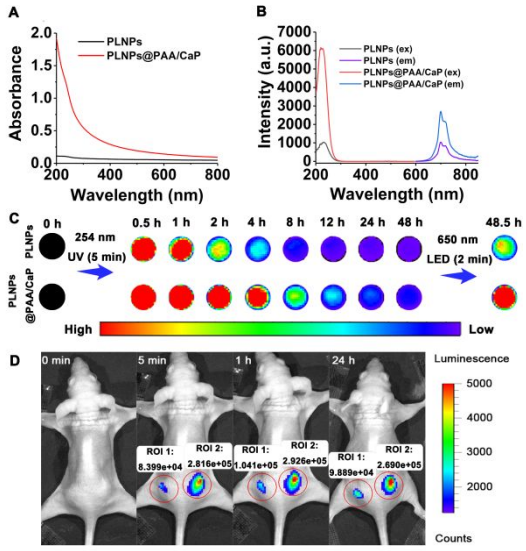

Fig. 3 (A) UV-vis absorption spectra of PLNPs (0.05 mg mL^{-1}) and PLNPs@PAA/CaP (0.05 mg mL^{-1} as PLNPs); (B) Excitation (em: 700 nm) and emission spectra (ex: 254 nm) of PLNPs (0.1 mg mL^{-1}) and PLNPs@PAA/CaP (0.1 mg mL^{-1} as PLNPs). (C) Images of the persistent luminescence of PLNPs (solid powder, 10 mg) and PLNPs@PAA/CaP (solid powder, 10 mg as PLNPs). PLNPs and PLNPs@PAA/CaP were excited by 254 nm UV light for 5 min, then the persistent luminescence images were recorded at different time points (0.5 h, 1 h, 2 h, 4 h, 8 h, 12 h, 24 h, and 48 h) after 254 nm UV light excitation stopped. Just after 48 h, the samples were recharged by a red LED for 2 min, and the images were obtained at 48.5 h. (D) In vivo afterglow imaging of a mouse. 0.2 mL PLNPs (left, 1 mg mL^{-1} in PBS) and 0.2 mL PLNP@PAA/CaP (right, 1 mg mL^{-1} as PLNPs in PBS) were injected subcutaneously into the back of the mouse, respectively.

Further efforts were made to understand the PAA/CaP induced enhancement of the persistent luminescence of PLNPs. PLNPs also suffer from high surface quenching effects as other luminescent nanoparticles due to high surface-to-volume ratio.[29,30] When PLNPs are prepared by doping luminescent center elements in the matrix, most of the doped ions are inevitably trapped by the outermost layer of the nanoparticles. However, the high-energy oscillators generated by ligands, surface impurities, and solvent molecules can easily extinguish the emission of surface dopants via a multi-phonon relaxation process.[31] In addition, the excitation energy of internal ions is likely transmitted to the surface quenching sites, leading to non-radiative relaxation. Covering the surface of nanomaterials with a heterogeneous shell structure is one of the effective means to solve the problem of surface quenching.[32] The shell can be used as an inert protective layer to protect the luminous center from harmful surface defects and any other quenchers in the adjacent environment, thereby significantly improving the luminous intensity of core-shell structure nanoparticles.[33] As a polyanionic polymer, the rich carboxyl groups in PAA can coordinate with metal ions and act as a "stationary" solvent. At this time, PAA becomes the matrix component of similar inorganic luminescent materials, so it can form luminescent nanomaterials with lanthanides.[34] Therefore, PAA may protect the luminescence center on the surface of PLNPs to enhance the overall luminescence of the material, which was also observed in other luminescent particles, such as $NaYF_4$: Yb^{3+}, Er^{3+}.[35]

PLNPs@PAA was also prepared for comparison with PLNPs@PAA/CaP to show the important role of PAA in the luminescence enhancement of PLNPs (Fig. S8A). Both PLNPs@PAA and PLNPs@PAA/CaP showed similar luminescence enhancement effect on PLNPs, indicating no obvious contribution of CaP in PAA/CaP shell to the luminescence enhancement of PLNPs (Fig. S8B-C). In other words, it is the PAA in PAA/CaP shell played a key role in the luminescence enhancement of PLNPs. The energy transfer from the PAA in PAA/CaP shell to PLNPs may contribute to the luminescence enhancement for PLNPs because of the significant overlap between the emission spectra of PAA and the absorption spectra of PLNPs (Fig. S8D).

Based on the above discussion, the mechanism for the PAA/CaP shell induced luminescence enhancement is illustrated in Fig. 4. The shell passivation mediated protection of the luminescence centers on the surface of PLNPs and the energy transfer between the PAA in the shell and PLNPs are the two main reasons for the enhancement of luminescence of PLNPs.

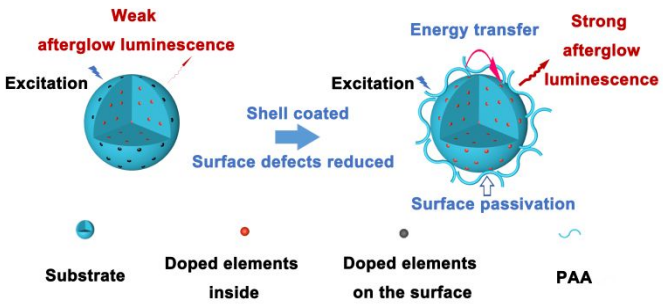

Fig. 4 Illustration of the mechanism for PAA induced enhancement of the afterglow luminescence of PLNPs by means of surface passivation and energy transfer.

Stability and drug loading/releasing performance of PLNPs@PAA/CaP

To evaluate its stability, PLNPs@PAA/CaP was dispersed in pH 7.4 PBS (10 mmol L^{-1}) and the phosphorescence spectra, hydrodynamic diameter, and FT-IR spectra of PLNPs@PAA/CaP were monitored within 30 days (Fig. S9A-C). No obvious changes of the phosphorescence spectra, hydrodynamic diameter, and FT-IR spectra of PLNPs@PAA/CaP were observed after dispersion in 30 days, indicating the good stability of PLNPs@PAA/CaP solution.

Water-soluble and positively charged DOX was used as a model antibacterial drug to evaluate the drug loading capacity of PLNPs@PAA/CaP. The large number of negatively charged carboxyl groups in PAA/CaP shell made the zeta potential of PLNPs decrease from +35.5 mV to -26.7 mV, so that large number of positively charged DOX could be loaded onto PLNPs@PAA/CaP. The loading of DOX increased the zeta potential of PLNPs@PAA/CaP to -12.0 mV (Fig. S10), enhanced the light absorption from 250 nm to 450 nm, and changed the color of PLNPs@PAA/CaP from white to yellow (Fig. S11A).

The capacity of PLNPs@PAA/CaP for DOX loading was determined

DOI: 10.1039/D3BM00142C

by UV–vis spectrophotometry. A large amount of DOX was quickly adsorbed by PAA/CaP within 1 h (Fig. S11B). The loading capacity and loading efficiency for DOX reached 428 μg mg^{-1} and 85.6%, respectively. Our PLNPs@PAA/CaP gave a significantly higher loading capacity than other previous systems for DOX.[36-38]

Further experiments were performed to reveal the infection microenvironment-responsive drug release behavior of PLNPs@PAA/CaP-DOX. Due to the acid degradation property of PAA/CaP shell, the time and pH-dependent release of DOX from PLNPs@PAA/CaP at 37°C was examined. PLNPs@PAA/CaP-DOX exhibited a much faster release profile of DOX in pH 5.5 PBS than in pH 7.4 PBS (Fig. 5A). The above results show the good drug delivery and release performance of PLNPs@PAA/CaP-DOX.

Antibacterial performance of PLNPs@PAA/CaP-DOX

MRSA, a pathogen of public health importance, was selected to explore the antibacterial ability of PLNPs@PAA/CaP-DOX by the plate counting method. The effect of the concentration of PLNPs@PAA/CaP-DOX on the antibacterial activity was tested in the concentration range of 0-20 μg mL^{-1}. The increase of PLNPs@PAA/CaP-DOX concentration made the bacterial colony survival rate decrease significantly (Fig. 5B and Fig. S12A). The bacterial growth was completely inhibited in the presence of 20 μg mL^{-1} PLNPs@PAA/CaP-DOX, but the bacteria grew significantly in the absence of PLNPs@PAA/CaP-DOX (control) (Fig. 5C). Fig. 5D and Fig. S12B show the growth of MRSA exposed to PLNPs@PAA/CaP-DOX for 24 h in the acidic and neutral environments. 20 μg mL^{-1} of PLNPs@PAA/CaP-DOX inhibited only 40% of MRSA at pH 7.4, but killed more than 99% of MRSA at pH 5.5. The live/dead fluorescent bacterial staining analysis also supported these results (Fig. S13). The above results show that PLNPs@PAA/CaP-DOX had the good performance of weak acidic bacterial infected microenvironment mediated drug release.

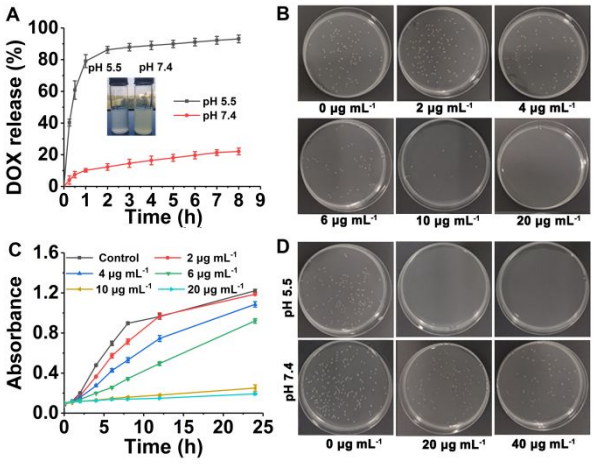

Fig. 5 (A) Sustained-release property of PLNPs@PAA/CaP-DOX in pH 5.5 and pH 7.4 PBS (insert: photographs of PLNPs@PAA/CaP-DOX incubated in pH 5.5 (left) and pH 7.4 (right) PBS); (B) Photographs of bacterial colonies after treatment with different concentrations of PLNPs@PAA/CaP-DOX (pH 5.5); (C) Time-dependent absorbance (600 nm) of bacterial suspensions treated with different concentrations of PLNPs@PAA/CaP-DOX; (D) Photographs of bacterial colonies after treatment with different concentrations of PLNPs@PAA/CaP-DOX (pH 7.4 and pH 5.5).

Cytotoxicity, hemocompatibility and biodistribution of PLNPs@PAA/CaP

The cytotoxicity of PLNPs@PAA/CaP was examined by the MTT assay. PLNPs@PAA/CaP did not show significant cytotoxicity after 24 h incubation with 3T3 cells even at a high concentration of 500 μg mL^{-1} (Fig. S14). Hemolysis test showed that the erythrocyte hemolysis rate of mouse blood in the presence of 500 μg mL^{-1} PLNPs@PAA/CaP was 1%, indicating good hemocompatibility of PLNPs@PAA/CaP (Fig. S15). These results indicate that PLNPs@PAA/CaP had good biocompatibility as a drug carrier in the treatment of bacterial infection.

To investigate the bio-distribution of PLNPs@PAA/CaP in mice, PLNPs@PAA/CaP-DOX was injected into normal mice through the tail vein. After 24 h of injection, the main organs such as heart, lung, liver, spleen, and kidney were taken out and irradiated with a LED light. In vitro luminescence imaging of these organs was performed 2 min after LED irradiation. The lung and liver showed the strongest afterglow signals, followed by the spleen, but the heart and kidneys gave no luminescence signal (Fig. S16). The results indicate that PLNPs@PAA/CaP-DOX mainly distributed in the lung and liver, followed by the spleen.

In vivo afterglow imaging and antibacterial therapy

The performance of PLNPs@PAA/CaP-DOX for in vivo afterglow imaging was evaluated by injecting PLNPs@PAA/CaP-DOX into the infected mice through the tail vein. The performance of PLNPs@PAA/CaP-DOX for in vivo afterglow imaging was evaluated by injecting PLNPs@PAA/CaP-DOX into the infected mice through the tail vein. The afterglow signal was observed nearly in the whole body after injection. The afterglow signal was observed nearly in the whole body at 5 min, 30 min, and 1 h injection. After that, the afterglow signal was obviously accumulated in the bacteria-infected area at 12 h, and lasting at 24 h, indicating PLNPs@PAA/CaP-DOX was accumulated to the infected area for targeted imaging of bacterial infection due to the EPR effect (Fig. 6A and Fig. S17).[39-41]

View Article Online
DOI: 10.1039/D3BM00142C

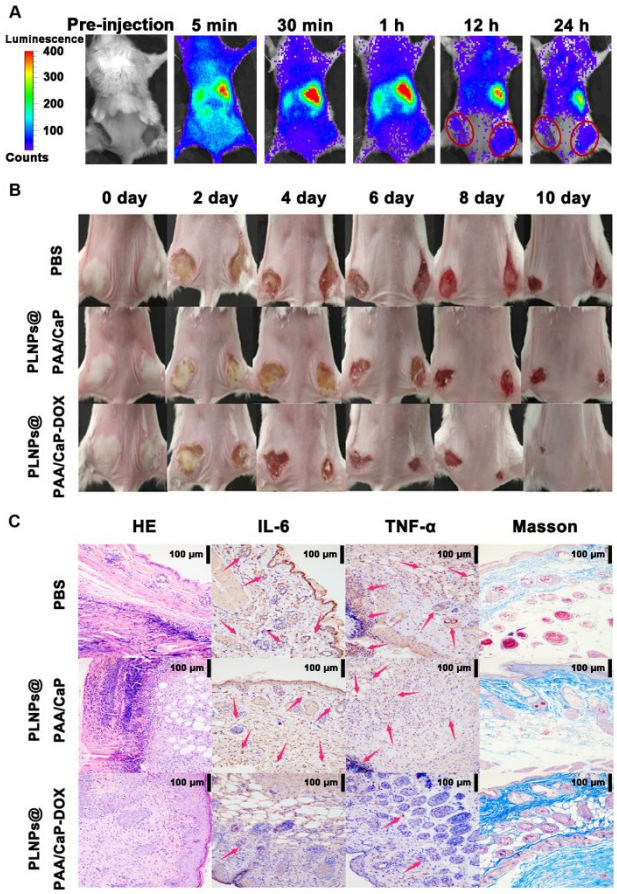

Fig. 6 (A) In vivo afterglow images of MRSA-infected mice at different times (5 min, 30 min, 1 h,12 h and 24 h) after injection of PLNPs@PAA/CaP-DOX; (B) Photographs of MRSA-infected mice after different treatments for 0, 2, 4, 6, 8, and 10 days; (C) H&E, Masson, IL-6, and TNF-α staining for histological examination of the skin tissue slices. Positive areas are marked with red arrows.

We further tested the capability of PLNPs@PAA/CaP-DOX for in vivo antibacterial therapy. Fig. 6B shows the photos of the tested mice under different treatments and the volume of abscesses in the tested mice over 10 days. The MRSA-infected mice in the PBS group and PLNP@PAA/CaP group exhibited severe suppuration and ulceration at the abscess site, and the infected area was still about 25% of the original abscess area on the 10th day (Fig. S18). In contrast, the infected area of the MRSA-infected mice in the PLNPs@PAA/CaP-DOX group almost disappeared, indicating the good capability of PLNPs@PAA/CaP-DOX for antibacterial therapy. PLNPs@PAA/CaP-DOX group showed a better therapeutic effect than the DOX-only treatment group (Fig. S19A-B) due to the accumulation and sustained release of DOX in PLNPs@PAA/CaP-DOX at the wound site. Moreover, free drug is more easily removed or inactivated by body fluids, resulting in a reduced therapeutic effect. The results are consistent with previous studies using calcium phosphate nanoparticles as a drug delivery system.[42]

To further evaluate the treatment effect of PLNPs@PAA/CaP-DOX, the infected sites of the mice were collected for hematoxylin-eosin (H&E) staining, Masson trichrome staining, and immunohistochemistry staining. As shown in Fig. 6C, large numbers of inflammatory cells and disorganized granulation tissue were seen in the PBS group, whereas a significant reduction in inflammatory cells, the well-organized epithelial layer, and the dermis with large number of blood vessels were observed in the PLNPs@PAA/CaP-DOX group. The immunohistochemical staining results of tumor necrosis factor-α (TNF-α) and interleukin-6 (IL-6) showed that they were only slightly expressed in the PLNPs@PAA/CaP-DOX group, but highly expressed in the PBS and PLNP@PAA/CaP groups. The results indicate that the treatment of PLNPs@PAA/CaP-DOX significantly improved the symptoms of inflammation.

The major organs of the mice in all groups were collected after treatment for H&E staining to evaluate the side effect of PLNPs@PAA/CaP-DOX. Compared with the PBS group, no obvious pathological tissue damage or abnormality was observed after intravenous injection of PLNPs@PAA/CaP or PLNPs@PAA/CaP-DOX (Fig. S20). Furthermore, the injection of PLNPs@PAA/CaP or PLNPs@PAA/CaP-DOX did not significantly affect the body weight of the mice (Fig. S21). These findings suggest that PLNPs@PAA/CaP had good biocompatibility without acute toxicity.

Conclusion

In conclusion, we have shown a persistent luminescence enhanced drug-loaded imaging nanoplatform PLNPs@PAA/CaP for imaging guided infection therapy. The passivation of the surface defects of

PLNPs by the shell and the energy transfer between the shell and PLNPs effectively prolong the decay time and enhance the sustained luminescence intensity of PLNPs. The excellent NIR-emitting afterglow of the nanoplatform allows autofluorescence-free bioimaging, while the mesoporous and acid-degradable structure of PAA/CaP on the surface of PLNPs not only gives high drug loading capacity, but also enables pH-responsive antibiotic release and bacterial infection therapy. Integrating the good signal penetrability and spontaneous fluorescence interference-free nature of NIR-emitting PLNPs to the interesting luminescence enhancement phenomenon of PAA/CaP shell provides an ideal nanoplatform for amplified NIR afterglow bioimaging along with the chemotherapy of bacterial infection.

Conflicts of interest

There are no conflicts to declare.

Author Contributions

Xuan Fu: conceptualization, investigation, validation, methodology, data curation, formal analysis, writing- original draft. Xu Zhao, Li-Jian Chen, Piming Ma and Tianxi Liu: methodology and formal analysis. Xiu-Ping Yan: conceptualization, supervision, funding acquisition, writing- review & editing. All authors have read and approved the final submitted manuscript.

Acknowledgments

The authors appreciate the financial support from the National Natural Science Foundation of China (No. 21934002), and the Collaborative Innovation Center of Food Safety and Quality Control in Jiangsu Province.

Notes and references

1 B. M. Liu, R. Zou, S. Q. Lou, Y. F. Gao, L. Ma, K. L. Wong and J. Wang, *Chem. Eng. J.*, 2021, **404**, 127133.
2 J. L. Li, J. Q. Guo, H. Li, J. L. Qu and J. Song, *Chem. Eng. J.*, 2021, **406**, 126008.
3 Y. Y. Xia, H. Y. Bao, J. Huang, X. D. Li, C. G. Yu, Z. J. Zhang and H. S. Wang, *Biomater. Sci*, 2020, **8**, 3095-3105.
4 J. Wang, Q. Q. Ma, W. Zheng, H. Y. Liu, C. Q. Yin, F. B. Wang, X. Y. Chen, Q. Yuan and W. H. Tan, *ACS Nano*, 2017, **11**, 8185-8191.
5 N. Liu, J. P. Shi, Q. Wang, J. R. Guo, Z. Y. Hou, X. H. Su, H. W. Zhang and X. L. Sun, *Small*, 2020, **16**, 2001494.
6 B. Yu, Y. J. Wang, Y. Y. Lin, Y. Feng, J. Wu, W. S. Liu, M. Wang and X. P. Gao, *Nanoscale*, 2022, **14**, 8978-8985.
7 Z. H. Wang, J. M. Liu, C. Y. Li, D. Wang, H. Lv, S. W. Lv, N. Zhao, H. Ma and S. Wang, *ACS Appl. Mater. Interfaces*, 2019, **11**, 36409-36419.
8 Y. F. Gao, R. Zou, G. F. Chen, B. M. Liu, Y. Zhang, J. Jiao, K. L. Wong and J. Wang, *Chem. Eng. J.*, 2021, **420**, 130021.
9 P. Lin, J. P. Shi, L. Y. Ming, Y. Y. Sheng, L. Song, M. C. Hong and Y. Zhang, *Chem. Eng. J.*, 2022, **442**, 135638.
10 D. D. Ding, S. Li, H. Xu, L. C. Zhu, S. S. Meng, J. Liu, Q. Lin, S. W. Leung, W. J. Sun, Y. M. Li and H. M. Chen, *ACS Appl. Mater. Interfaces,* 2021, **13**, 16166-16172.
11 L. X. Yan, L. J. Chen, X. Zhao and X. P. Yan, *Adv. Funct. Mater.*, 2020, **30**, 1909042.
12 K. Huang, Z. J. Li, Y. Li, N. Yu, X. P. Gao, L. Huang, S. F. Lim and G. Han, *Nano Lett.*, 2021, **21**, 4903-4910.
13 H. X. Zhao, G. Shu, J. Y. Zhu, Y. Y. Fu, Z. Gu and D. Y. Yang, *Biomaterials*, 2019, **217**, 119332.
14 H. J. Zhang, X. Zhao, L. J. Chen, C. X. Yang and X. P. Yan, *Anal. Chem*., 2020, **92**, 1179-1188.
15 J. W. Zhao, Z. P. Zhang and X. Wang, *J. Alloys Compd*., 2020, **820**, 153142.
16 E. Palo, S. Lahtinen, H. Pakkila, M. Salomaki, T. Soukka and M. Lastusaari, *Langmuir*, 2018, **34**, 7759-7766.
17 B. Liu, Y. Y. Chen, C. X. Li, F. He, Z. Y. Hou, S. S. Huang, H. M. Zhu, X. Y. Chen and J. Lin, *Adv. Funct. Mater*., 2015, **25**, 4717-4729.
18 L. H. Fu, Y. R. Hu, C. Qi, T. He, S. Jiang, C. Jiang, J. He, J. Qu, J. Lin and P. Huang, *ACS Nano*, 2019, **13**, 13985-13994.
19 Z. Q. Wang, L. C. Wang, N. Prabhakar, Y. X. Xing, J. M. Rosenholm, J. X. Zhang and K. Y. Cai, *Acta Biomater*., 2019, **86**, 416-428.
20 S. K. Liu, W. T. Li, S. M. Dong, S. L. Gai, Y. S. Dong, D. Yang, Y. L. Dai, F. He and P. P. Yang, *ACS Appl. Mater. Interfaces*, 2019, **11**, 47659-47670.
21 X. Wang, M. J. Zhang, L. Y. Zhang, L. Li, S. N. Li, C. G. Wang, Z. M. Su, Y. Yuan and W. S. Pan, *Chem. - Eur. J.*, 2017, **23**, 6586-6595.
22 L. Li, L. Y. Zhang, T. T. Wang, X. T. Wu, H. Ren, C. G. Wang and Z. M. Su, *Small*, 2015, **11**, 3162-3173.
23 X. Zhao, K. C. Zhao, L. J. Chen, Y. S. Liu, J. L. Liu and X. P. Yan, *Chem. Sci*., 2021, **12**, 442-452.
24 H. Z. Shi, L. Li, L. Y. Zhang, T. T. Wang, C. G. Wang, D. X. Zhu and Z. M. Su, *CrystEngComm*, 2015, **17**, 4768-4773.
25 J. G. Acheson, L. Robinson, S. McKillop, S. Wilson, M. J. McIvor, B. J. Meenan and A. R. Boyd, *Mater. Charact.*, 2021, **171**, 110739.
26 T. Y. Wang, D. Dong, T. Chen, J. J. Zhu, S. X. Wang, W. Wen, X. H. Zhang, H. D. Tang, J. C. Liang, S. F. Wang and H. Y. Xiong, *Chem. Eng. J.*, 2022, **446**, 137172.
27 L. X. Shi, J. J. Shao, X. H. Jing, W. W. Zheng, H. Liu and Y. Zhao, *ACS Sustain. Chem. Eng*., 2020, **8**, 686-694.
28 M. Y. Shi, S. K. Lan, C. Zhang, W. Z. Xiong, Q. Li, T. Maimaiti, F. S. Liu, C. Z. Liang, X. Wu and S. T. Yang, *Colloids Surf. B.,* 2021, **205**, 111887.
29 Y. Bai, M. M. Hao, S. S. Ding, P. Chen and L. Z. Wang, *Adv. Mater*., 2022, **34**, 2105958.
30 W. Bian, Y. Lin, T. Wang, X. Yu, J. Qiu, M. Zhou, H. Luo, S. F. Yu and X. Xu, *ACS Nano*, 2018, **12**, 3623-3628.
31 S. V. Kilina, P. K. Tamukong and D. S. Kilin, *Acc. Chem. Res.*, 2016, **49**, 2127-2135.
32 K. Huang, M. K. G. Jayakumar and Y. Zhang, *J. Mater. Chem. C*, 2015, **3**, 10267-10272.
33 P. Pei, Y. Chen, C. X. Sun, Y. Fan, Y. M. Yang, X. Liu, L. F. Lu, M. Y. Zhao, H. X. Zhang, D. Y. Zhao, X. G. Liu and F. Zhang, *Nat. Nanotechnol.*, 2021, **16**, 1011-1018.
34 A. Rosendo, M. Flores, G. Córdoba, R. Rodŕıguez and R. Arroyo, *Mater. Lett*., 2003, **57**, 2885-2893.
35 E. Palo, M. Salomaki and M. Lastusaari, *J. Colloid Interface Sci.,* 2017, **508**, 137-144.
36 N. Labban, H. N. Al-Otaibi, A. Binrayes, A. S. Aljamhan, A. F. Alfouzan, S. M. Al Taweel and M. K. Assery, *Int. J. Adhes Adhes*, 2021, **111**, 102975.
37 A. M. Alswieleh, *J. Chem.*, 2020, **2020**, 9176257.
38 M. Deaconu, I. Nicu, R. Tincu, A. M. Brezoiu, R. A. Mitran, E. Vasile, C. Matei and D. Berger, *Chem. Zvesti*, 2018, **72**, 1869-1880.
39 E. A. Azzopardi, E L. Ferguson and D. W. Thomas, *JAC,* 2013, **68**, 257-274.

View Article Online
DOI: 10.1039/D3BM00142C

40 Y. j. Liu, D. d. Sun, Q. Fan, Q. G. Ma, Z. L. Dong, W.W. Tao, H . Q . Tao, Z. Liu and C. Wang, *Nano Res*. 2020, **13**, 564-569.
41 A. G. Lin, Y. N. Liu, X. F. Zhu, X. Chen, J. W. Liu, Y. H. Zhou, X. Y. Qin and Ji. Liu, *ACS Nano*. 2019, **13**, 13965-13984.
42 R. Mukherjee, M. Patra, D. Dutta, M. Banik, T. Basu, Biochim. Biophys. *Acta, Gen. Subj*. 2016, **9**, 1929-1941.